RSC Sustainability

ROYAL SOCIETY OF CHEMISTRY

PAPER

View Article Online
View Journal | View Issue

Check for updates

Cite this: *RSC Sustainability*, 2026, **4**, 404

An eggshell-derived $CaCO_3$ porous carbon-based nanocomposite for cancer therapy

Qicang Wang,†[ab] Jiayi Chen,†[a] Jiawei Chen,[a] Qiuping Wu,[a] Xinyu Yang,[a]
Shaowei Wang,[c] Shijun Xing,[a] Chen Chen,[a] Wenping Li *[a] and Jiazhi Yang[a]

Received 8th September 2025
Accepted 18th November 2025

DOI: 10.1039/d5su00732a

rsc.li/rscsus

Cancer therapy faces challenges including poor targeting, systemic toxicity, and inefficient drug release. To address these, we developed an eco-friendly drug delivery system using eggshell-derived calcium carbonate ($CaCO_3$). Porous C-PEG@ES nanoparticles were fabricated *via* PEG-assisted carbonization at 600 °C, exhibiting high specific surface area and pH-responsive drug release. In an acidic tumor microenvironment (pH 5.5), $CaCO_3$ decomposition enhanced oxaliplatin release, showing 2.3-fold higher efficiency than at pH 7.4. The system also raised environmental pH from 5.2 to 6.2 within 15 hours, modulating the tumor microenvironment and promoting apoptosis. Cytotoxicity tests confirmed its biocompatibility and antitumor efficacy, offering a sustainable and precise therapeutic strategy with reduced systemic toxicity.

Sustainability spotlight

This study converts waste eggshells into value-added drug carriers through calcium carbonate extraction, PEG modification, and carbonization. It mitigates environmental pressure from eggshell disposal, reduces reliance on mined calcium carbonate, and offers a green, low-toxicity, and biocompatible alternative for drug delivery systems. The work clearly aligns with UN Sustainable Development Goals (SDG 12: Responsible Consumption and Production; SDG 9: Industry, Innovation and Infrastructure), promoting the integration of circular economy principles and green pharmaceutical development.

1. Introduction

Cancer remains one of the most formidable threats to global health. As a leading cause of death worldwide, cancer results in nearly 10 million deaths annually, as reported by the World Health Organization.[1–3] Early diagnosis and treatment are essential to improve survival rates and reduce treatment costs for cancer patients, thus requiring advanced therapeutic strategies to meet the challenges.[4,5] Current mainstream cancer therapies primarily include surgical resection, radiotherapy, and chemotherapy.[6,7] While surgery is effective for localized tumors, it fails to address metastatic lesions.[8] Radiotherapy and chemotherapy, though systemic in action, often cause severe damage to healthy tissues due to their non-specific targeting, leading to complications such as immunosuppression and organ toxicity.[9,10] Among these modalities, chemotherapy is widely regarded as the most versatile and effective approach for advanced or disseminated cancers.[11] However, conventional chemotherapeutic agents suffer from limitations such as poor solubility, rapid clearance, and off-target effects, which significantly compromise therapeutic efficacy and patient survival.[12,13] To address these challenges, drug delivery systems (DDS) have emerged as a critical strategy to enhance drug bioavailability and reduce systemic toxicity.[14–17]

Various nanocarriers, including liposomes, polymeric micelles, and inorganic nanoparticles, have been explored for their ability to encapsulate and deliver chemotherapeutics.[18,19] Notably, calcium carbonate ($CaCO_3$) nanoparticles have garnered increasing attention due to their excellent biocompatibility, pH-responsive degradation in the acidic tumor microenvironment, and high drug-loading potential. The inherent ability of $CaCO_3$ to dissolve in acidic tumor microenvironments enables targeted drug release, while its degradation products (CO_3^{2-}) can neutralize acidic conditions, potentially inhibiting tumor invasion and metastasis.[20–22] For instance, Chen *et al.* successfully synthesized pH-responsive hyaluronate-$CaCO_3$ hybrid particles, which demonstrated remarkable stability under physiological conditions while achieving rapid doxorubicin (DOX) release specifically within the acidic tumor microenvironment.[23] Furthermore, $CaCO_3$-based nanocarriers enable synergistic antitumor strategies through their pH-responsive degradation. These systems can simultaneously

---

[a] *School of Chemistry and Chemical Engineering, Nanjing University of Science and Technology, 200 Xiao Ling Wei Street, Nanjing, Jiangsu Province, 210094, China. E-mail: lwp@njust.edu.cn; Tel: +86-15251893282*

[b] *Jiangsu Fangyang Water Co., Ltd, No.499 Jiangsu Avenue, Xuwei New District, Lianyungang, Jiangsu province, China*

[c] *Yantai Ecological Environment Monitoring Center of Shandong Province, Yantai, Shandong, 264000, China*

† These authors contributed to this manuscript equally.

modulate the tumor microenvironment to enhance immunotherapy, initiate calcium overload for apoptosis, and when combined with photothermal agents, achieve combined chemo-photothermal therapy, offering comprehensive treatment through multimodal integration.[24–27]

In the field of cancer therapy, conventional drug delivery systems often struggle to balance therapeutic efficacy with ecological sustainability due to non-biodegradability, high toxicity, and environmental residue issues. To address this, green nanomaterials, such as carriers derived from natural polymers or biowaste, have gained significant attention for their biocompatibility, low environmental impact, and green synthesis pathways. Particularly noteworthy are biowaste-derived pH-responsive carriers, which not only enable targeted drug release in the tumor microenvironment but also transform waste materials such as shrimp shells and eggshells into high-value medical resources, aligning precision treatment with circular economy principles.[28–31] Notably, our strategy focuses on developing eco-friendly $CaCO_3$ carriers derived from biomass waste, specifically eggshells (ES). Comprising 95% $CaCO_3$, eggshells represent an underutilized resource whose improper disposal may lead to substantial environmental burdens.[32,33] Previous studies have demonstrated the potential of ES-derived materials in biomedical applications. Piyachat Chuysinuan *et al.* demonstrated the conversion of eggshells into hydroxyapatite (HA) for dental tissue engineering, successfully preparing a fibroin-alginate injectable hydrogel incorporating eggshell-derived HA with alveolar bone resemblance functions as advanced dental scaffolding.[34] In contrast to such structural biomimicry approaches, our strategy innovatively repurposes eggshell-derived biogenic calcium carbonate ($CaCO_3$) for tumor-targeted drug delivery. Rather than converting $CaCO_3$ to HA for enhanced osteoconductivity, we preserve its innate crystalline structure and leverage its intrinsic pH-responsive behavior to construct a stimuli-responsive drug carrier. Shafiu Kamba *et al.* developed pH-sensitive $CaCO_3$ nanocrystal carriers with enhanced doxorubicin (DOX) loading capacity compared with traditional vaterite $CaCO_3$.[35] However, despite this advancement, the nanocrystals maintained a dense structures, which kind of hindered efficient drug encapsulation. This limitation necessitates innovative surface modification strategies to optimize their physicochemical and biological performance.

Recent advancements in nanomaterial engineering have identified polyethylene glycol (PEG) as a versatile surface modifier. PEGylation has proven effective in enhancing nanoparticle stability, prolonging blood circulation time, and reducing immune clearance. Furthermore, PEG modification improves biocompatibility and alters organ-specific accumulation patterns, thereby minimizing systemic toxicity.[36,37] Sanyog Jain *et al.* improved biocompatibility of carbon nanotubes(CNTs) through PEGylation. Adopting these functionalization strategies may optimize drug stability and treatment efficacy for CNTs and related nanocarriers in the future.[36] While conventional PEGylation strategies primarily focus on surface coating to improve pharmacokinetics, our strategy advances conventional PEGylation by transforming PEG from a surface modifier into a sacrificial structural component. Through carbonization at 600 °C, the PEG layer decomposes into a porous carbon framework while re-exposing $CaCO_3$ surfaces, creating a unique hybrid architecture. This carbon-$CaCO_3$ composite enables dual drug-loading through carbon pore adsorption and ionic interactions, achieving enhanced drug delivery performance beyond traditional PEGylated systems.

While eggshell-derived materials offer sustainable advantages, their translation into clinically viable nanomedicines requires careful consideration of standardization and regulatory compliance. To translate eggshell-based carriers into clinical nanomedicines, we have developed a standardized protocol: sourcing eggshells uniformly from food processing plants, ensuring material purity through rigorous cleaning and thermal treatment, and maintaining fixed production parameters such as carbonization temperature to achieve consistent pore structure and composition across batches. Continuous monitoring of safety indicators like calcium content and heavy metals, along with stability validation under various conditions, is implemented. This approach preserves the eco-friendly attributes of eggshells while meeting pharmaceutical production standards through quantifiable quality control, establishing a reliable foundation for clinical application and regulatory approval.

Herein, we prepared a novel PEG-modified $CaCO_3$ carrier featuring a loosely porous carbonaceous chrysalis-like structure. The obtained C-PEG@ES nanoparticles exhibit excellent pH-responsive behavior and tumor therapy effectiveness. Upon the obtained C-PEG@ES nanoparticles reaching tumor sites, the acidic microenvironment triggers $CaCO_3$ dissolution, accelerating drug release while simultaneously neutralizing pH of tumor environment to effectively prevent cancer cells from invading other normal cells. Importantly, by synergizing pH-responsive drug delivery with microenvironmental modulation, this platform holds dual potential for inducing cancer cell apoptosis and suppressing metastatic behavior. Such tumor-targeted drug delivery system overcomes the limitations of traditional chemotherapy and conventional $CaCO_3$ carriers, offering a promising strategy for precision oncology.

2. Experimental section

2.1 Materials

$CaCl_2$ was provided by Sinopharm Chemical Reagent Co., Ltd. Ethanol(99.5%) and NH_4HCO_3 was purchased from Shanghai Macklin Biochemical Co., Ltd. PEG600 was bought from Shanghai Lingfeng Chemical Reagent Co., Ltd. Eggshell were obtained from Suguo Supermarket.

2.2 Preparation of drug carriers and drug loading

Eggshells were crushed into ultrafine powder using a mortar and pestle, followed by sieving to obtain a homogeneous ES powder. A mixture of 0.4 g ES powder and 2 g PEG600 was added to a beaker containing 8 g deionized water. The suspension was ultrasonicated for 2 h and then stirred at 600 rpm for 10 h. The product was centrifuged, washed thoroughly, and freeze-dried to obtain PEG@ES. Subsequently, the obtained PEG@ES was subjected to carbonization at 600 °C for 2 h, yielding the final C-PEG@ES.

C-PEG@ES was dispersed in pure water. Subsequently, 5 mL of oxaliplatin (OXA) solution (2 mg mL^{-1}) was added into $CaCO_3$/CBCN solution. The mixture was continuously stirred at room temperature for 12 hours. The OXA-loaded C-PEG@ES composites were then collected by centrifugation.

2.3 Characterization

Morphological features of the samples were analyzed using a scanning electron microscope (JEM-6380LV, JEOL Ltd, Japan). Particle size distribution was measured at 25 °C using a Nanoparticle potential analyzer (Malvern, UK). Crystallographic properties were evaluated using a X-ray diffractometer (D8ADVANCE, Bruker, Germany) with Cu Kα radiation (λ = 0.151478 nm). Data were collected over a range of 5°to 80°, with operating parameters set to 40 kV(1 kV/1 step) and 40 mA. Chemical molecular structures were identified using a Fourier Transform Infrared Spectrometer (NICOLET iS10, Thermo Fisher Scientific Co., Ltd, USA). Spectra were recorded in the range of 400–4000 cm^{-1}. Surface elemental composition and chemical states were analyzed using a X-ray Photoelectron Spectroscopy (PHI Quanter, Ulvac-PHI, Japan) with an Al X-ray source. Measurements were performed under 10^{-8} Pa. Specific surface area and pore size distribution were determined using a surface area analyzer (ASAP 3020, USA). The specific surface area of the samples was calculated by the BET (Barren–Emmett–Teller) method and the pore size distribution was calculated by the BJH (Barrte–Joyner–Haland) equation.

2.4 *In Vitro* calcium ion and drug release

Calcium ion release profiles were investigated under simulated physiological conditions. C-PEG@ES nanoparticles were dispersed in phosphate-buffered saline (PBS, pH 7.4, 6.7, 6.2, or 5.0) to mimic normal tissue and tumor microenvironments. At predetermined time intervals, the suspensions were centrifuged, and the supernatants were collected to quantify calcium ion (Ca^{2+}) and pH.

The *in vitro* OXA release performance was investigated by incubating nanoparticles in phosphate-buffered saline (PBS, pH 7.4, 6.7, 6.2, or 5.0). At designed time points, the OXA released into the PBS solution was measured by UV-vis spectrophotometer.

C-PEG@ES-OXA nanoparticles were dispersed in PBS buffer containing 5% fetal bovine serum (FBS) and incubated at 37 °C with constant shaking for 24 h. The mixture was then centrifuged at 13 000 rpm for 10 min to separate the nanoparticles from the release medium. Then incubating nanoparticles in phosphate-buffered saline. Samples were taken at different time points, and the cumulative release of OXA was quantified by UV spectroscopy to evaluate its *in vitro* release performance under the influence of the protein corona.

2.5 Cell viability assay and live/dead double staining assay

We systematically evaluated the biocompatibility and antitumor efficacy of the C-PEG@ES nanomaterial using the following cell models: rat bone marrow mesenchymal stem cells (BMSCs) for biocompatibility, and colon carcinoma (CT26) and rat osteosarcoma (UMR-106) cells for antitumor activity. Cells were seeded in 96-well plates, BMSCs were cultured in DMEM high-glucose medium containing pristine C-PEG@ES nanoparticles, while CT26 and UMR-106 cells cultured in DMEM high-glucose medium containing oxaliplatin-loaded (C-PEG@ES-OXA) and doxorubicin-loaded (C-PEG@ES-DOX), respectively. All treatments were carried out for 24 and 48 hours. Subsequently, cell viability was assessed using the Cell-Titre-Glo®.3D. Luminescent Assay, and luminescence signals were measured with a microplate reader. The cell live/dead double staining assay was performed following the standard protocol of the Calcein-AM/PI Double Staining Kit.

3. Results and discussion

In this study, a green and sustainable strategy was developed to synthesize carbon-based nanocomposites (C-PEG@ES) using biomass materials as the raw material. As illustrated in Scheme 1, the natural calcium carbonate shell obtained from discarded eggshells was mechanically ground into homogeneous powder after removing the inner membrane. A facile one-step synthesis method was employed to coat the eggshell particles with polyethylene glycol (PEG). The obtained product underwent

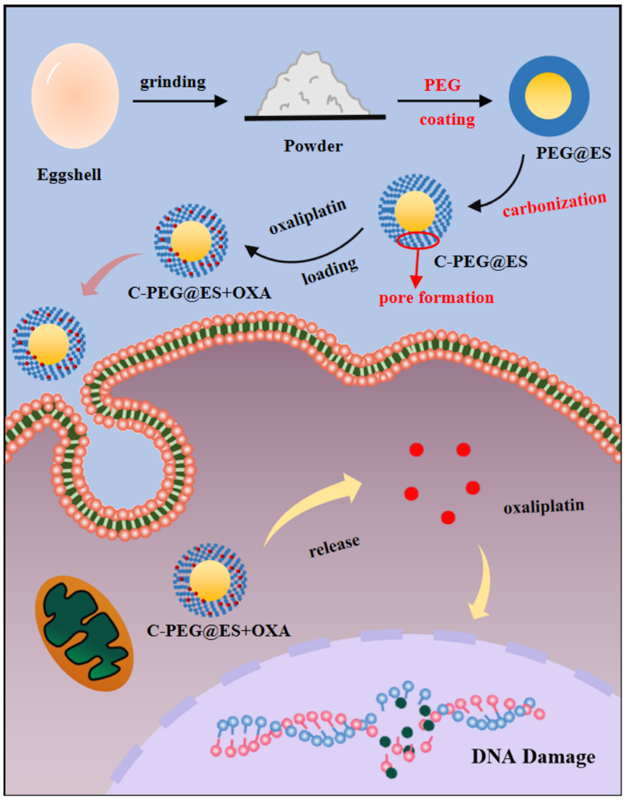

Scheme 1 Schematic illustration of C-PEG@ES.

centrifugal washing, freeze-drying, and subsequent carbonization at 600 °C for 2 h, the heating induces a partial decomposition of $CaCO_3$, with subsequent CO_2 release, which causes the formation of pores in the carbon residual layer after PEG decomposition, yielding a porous C-PEG@ES nanoparticles. The prepared nanocomposite exhibited a unique architecture, where the outer PEG-functionalized carbon layer provided abundant binding sites for efficient loading of antitumor drugs. The inherent calcium carbonate component can gradually decompose in the weakly acidic tumor microenvironment facilitated drug release, and this neutralization effect of calcium carbonate on acidic tumor regions can also contribute to microenvironment modulation, inhibiting cancer cell invasion and enhancing apoptosis. Besides, this approach significantly reduced material costs and environmental burdens through the utilization of biowaste, and the mild reaction conditions and simple operational procedures minimized energy consumption and potential toxicity risks. These findings highlight the potential of biomass materials as eco-friendly and multifunctional platforms for precision cancer therapy.

To determine the optimal carbonization temperature for the C-PEG@ES composite, materials were synthesized at different temperatures (500, 600, and 700 °C) and systematically characterized. Fig. 1a displays the N_2 adsorption–desorption isotherms of the samples prepared at each temperature. All three isotherms exhibit type-IV curves with distinct hysteresis loops, indicative of mesoporous structures. However, the sample carbonized at 500 °C shows only a weak hysteresis loop, suggesting limited mesopore development due to incomplete carbonization. In contrast, the isotherms of the 600 °C and 700 °C samples display well-defined hysteresis with comparable shapes and areas, implying that increasing the temperature from 600 to 700 °C does not lead to a significant enhancement in porosity. Pore size distribution curves derived from the adsorption data are presented in Fig. 1b. The sample prepared at 600 °C shows a average pore diameter of 15.5 nm, whereas the 500 °C sample exhibits a broader and less intense pore size profile. The 700 °C sample shows a similar pore size distribution to that treated at 500 °C, further confirming that no substantial structural improvement is achieved at the higher temperature. Based on these results, 600 °C was selected as the optimal carbonization temperature. Therefore, 600 °C provides an effective synthesis condition that ensures both suitable pore structure and preservation of functional components.

The surface morphology of ES and C-PEG@ES nanomaterials was characterized by scanning electron microscopy (SEM). As shown in Fig. 2, the ES nanoparticles exhibited a dense structure with partial surface protrusions and an average particle size of approximately 300 nm. This compact morphology suggests that pristine eggshell materials (ES) are unsuitable for direct application as drug carriers. In contrast, the C-PEG@ES nanoparticles displayed an irregular shape with a loose and highly porous structure in Fig. 2. This porous architecture provides abundant active sites for the loading of antitumor drugs such as doxorubicin (DOX), preliminarily confirming the successful synthesis of the C-PEG@ES nanomaterial (Fig. 2).

Further hydrodynamic size analysis *via* dynamic light scattering (DLS) revealed that the average particle sizes of ES and C-PEG@ES were approximately 380 nm and 410 nm, respectively in Fig. 3a. The slight increase in size after PEG modification and carbonization aligns with the formation of a surface coating during the synthesis process. Notably, the hydrodynamic diameters measured by DLS were larger than the dimensions observed in SEM images, which may be attributed to the hydration effect of nanoparticles in aqueous environments, leading to particle swelling or aggregation.

The crystalline structures of ES, PEG@ES, and C-PEG@ES were analyzed by X-ray diffraction (XRD). As shown in Fig. 3b, the pristine ES pattern confirms well-crystallized calcite $CaCO_3$. Following PEG modification, the remarkable attenuation of $CaCO_3$ diffraction peaks demonstrates effective surface coating. After carbonization, the C-PEG@ES pattern shows reappearance and intensification of certain $CaCO_3$ peaks, indicating structural reorganization and pore formation which can enhance drug loading capacity through increased surface area. Simultaneously, the emergence of CaO phases confirms partial

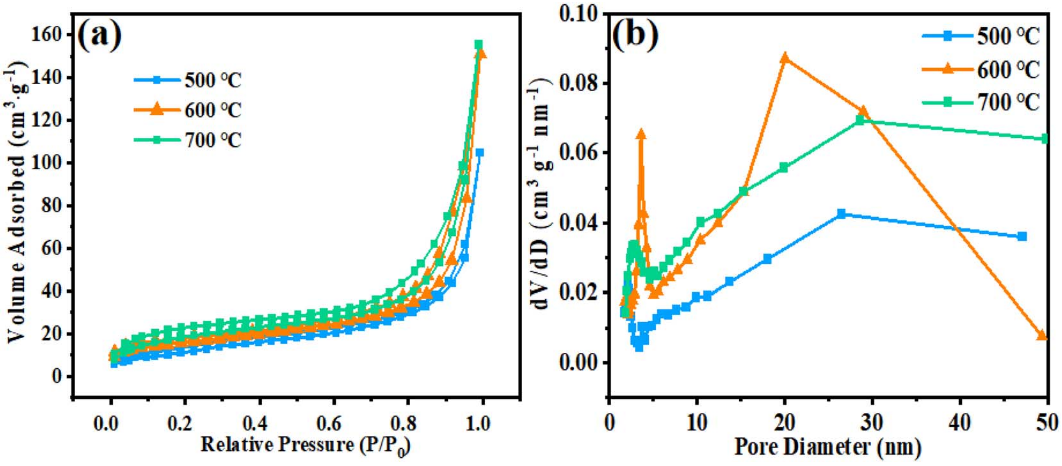

Fig. 1 (a) Nitrogen adsorption–desorption isotherms, (b) distribution curves.

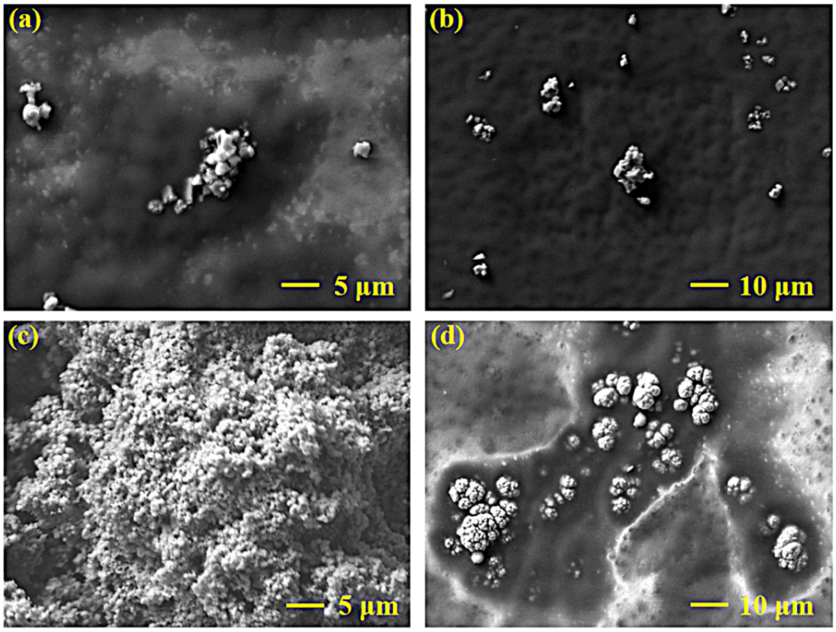

Fig. 2 SEM images of ES (a and b) and C-PEG@ES (c and d).

decomposition of $CaCO_3$ under thermal treatment. Most notably, the graphitic carbon peak at approximately 28° provides conclusive evidence of successful carbonization, forming a stable carbon framework. These transformations collectively verify the formation of a hybrid nanocomposite wherein the restructured $CaCO_3$ enables pH-triggered drug

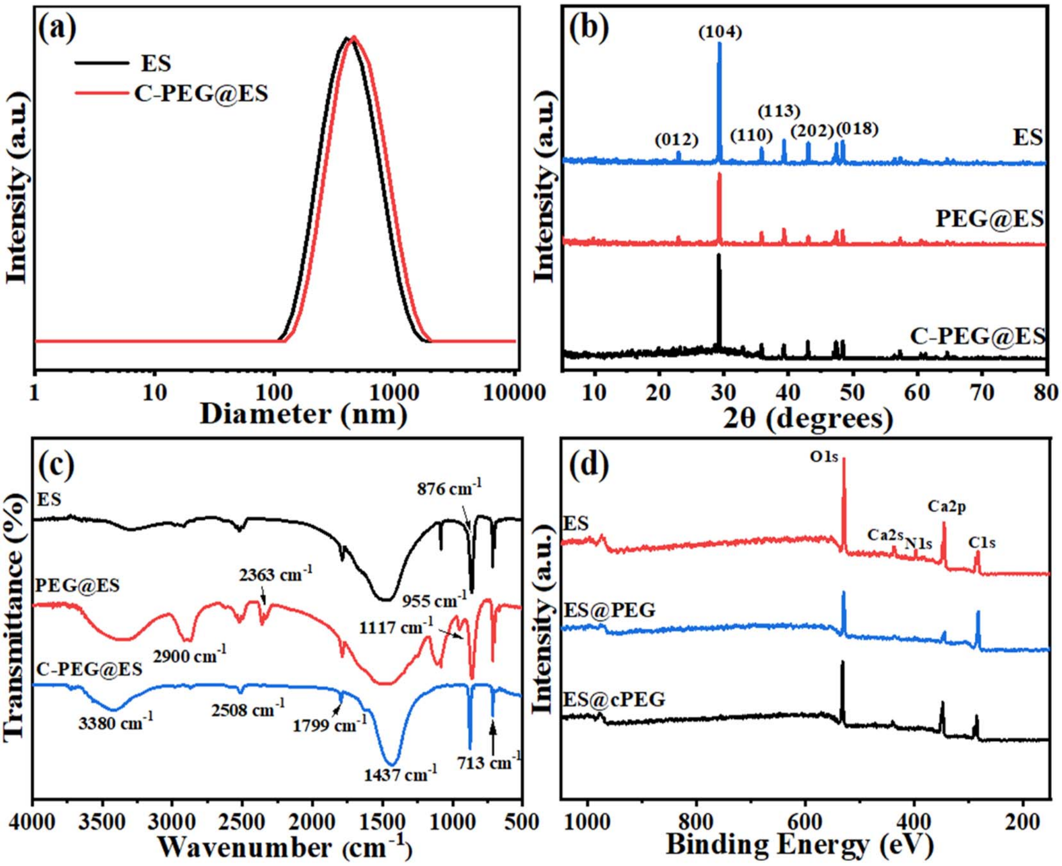

Fig. 3 (a) Size distribution, (b) XRD patterns, (c) FTIR spectra, (d) XPS spectra.

release in acidic tumor microenvironments, while the carbonaceous matrix ensures structural stability. The synergistic combination of these structural features results in significantly improved drug loading capacity and controlled release properties, making the composite particularly suitable for tumor therapy applications.

The chemical structure composition of ES, PEG@ES, and C-PEG@ES were further investigated using Fourier-transform infrared (FTIR) spectroscopy in Fig. 3c. The spectrum of pristine eggshell (ES) displayed characteristic calcite $CaCO_3$ absorptions, including vibrations at 1799 cm^{-1} and 1437 cm^{-1}. Successful PEG modification was confirmed by emerging vibrational modes at 3380 cm^{-1} (–OH), 2900 cm^{-1} (C–H), and 1117 cm^{-1} (C–O–C). The carbonization process induced profound structural transformations in C-PEG@ES, characterized by the complete disappearance of PEG fingerprints and attenuation of carbonate bands, indicating thermal decomposition and structural rearrangement. These transformations directly enhance the material's drug delivery functionality. The decomposition of organic components creates a porous architecture that significantly increases specific surface area, providing abundant active sites for drug loading. The preserved $CaCO_3$ maintain pH-responsive characteristics, enabling targeted drug release in acidic tumor microenvironments. The synergistic combination of these structural features results in substantially improved drug loading capacity and controlled release properties, making the nanocomposite particularly suitable for tumor therapy.

The chemical compositions of ES, PEG@ES, and C-PEG@ES were analyzed by X-ray photoelectron spectroscopy (XPS), as shown in Fig. 3d. For pristine ES, its primary components are calcium carbonate ($CaCO_3$) and proteins corresponding to the characteristic peaks at 283 eV (C1s), 348 eV (Ca2p), 438 eV (Ca2s), 529 eV (O1s), and 397 eV (N1s) respectively. The presence

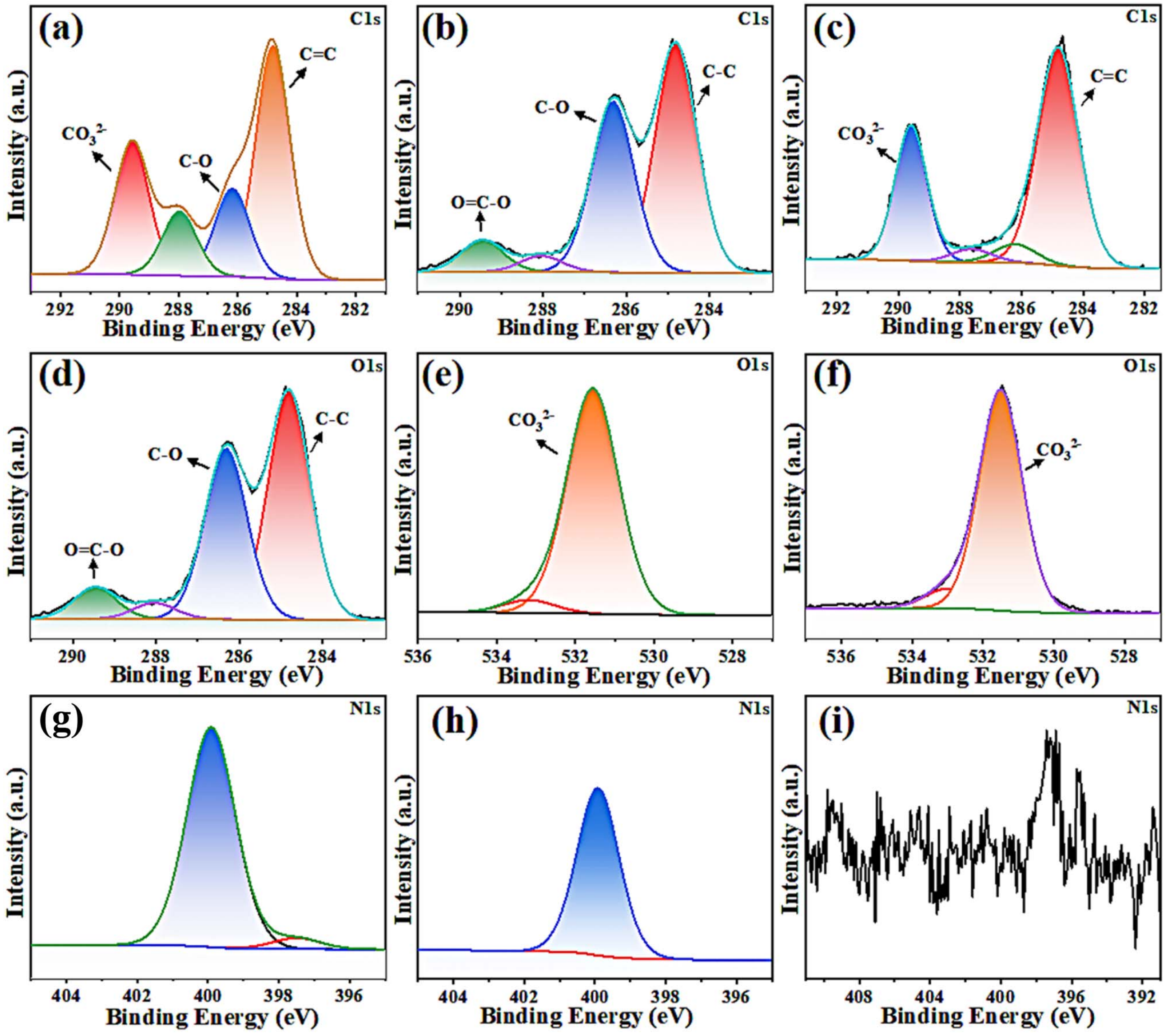

Fig. 4 High-resolution (a–c) C1s, (d–f) O1s, and (g–i) N1s spectra of ES, PEG@ES, and C-PEG@ES.

of the N1s peak further confirms the existence of proteinaceous components in ES. Upon PEG modification (PEG@ES), the Ca2s and N1s peaks nearly disappeared, while the Ca2p peak intensity significantly decreased. This observation suggests the successful loading of PEG onto ES, which shielded the internal $CaCO_3$ and protein components. Interestingly, in the C-PEG@ES nanocomposite, the Ca2p (348 eV) and Ca2s (438 eV) peaks reappeared, indicating that the carbonization process induced a porous and loosened structure in the surface PEG layer, thereby re-exposing the internal $CaCO_3$. This observation demonstrates not only the successful loading of PEG onto ES but also the formation of a porous architecture after carbonization. The generated porous framework provides abundant active sites for the loading of anticancer drugs such as doxorubicin (DOX), confirming the successful preparation of the designed composite material.

To further investigate the loading efficiency of PEG, the chemical environment of ES, PEG@ES, and C-PEG@ES were analyzed by high-resolution XPS spectra. Fig. 4a–c displays the C1s high-resolution spectra of the three samples. For pristine ES, the C1s spectrum reveals characteristic peaks corresponding to CO_3^{2-}, O═C–O, C–O, and C–C, consistent with its $CaCO_3$ and protein composition. After PEG modification (PEG@ES), the intensities of the CO_3^{2-} and O═C–O peaks significantly decreased, while the C–O peak intensified, indicating the effective coverage of ES by PEG. Notably, upon carbonization (C-PEG@ES), the O═C–O and C–O peaks nearly vanished, accompanied by a marked enhancement of the CO_3^{2-} peak. This observation suggests that the carbonization process induced a porous structure in the PEG layer, re-exposing the underlying $CaCO_3$. The O1s spectral evolution in Fig. 4d–f further corroborates the successful loading and carbonization of ES by PEG. After PEG modification (PEG@ES), the CO_3^{2-} peak was obscured, and the C═O peak dominated. After carbonization, the CO_3^{2-} peak intensity enhanced, whereas the O═C–O and C–O peaks diminished drastically, confirming the removal of PEG and the re-emergence of $CaCO_3$. The nitrogen element, primarily originating from proteins in the eggshell (ES), also exhibited significant changes. As shown in Fig. 4g–i, the N1s peak intensity decreased sharply after PEG encapsulation, implying shielding of protein components by the PEG layer. Following carbonization, the N1s signal almost disappeared, which can be attributed to the thermal decomposition of proteinaceous biomolecules during high-temperature treatment. The structural transformations create significant advantages for drug delivery. The carbonized PEG forms a porous network that enables drug adsorption through π–π stacking and hydrophobic interactions, while the re-exposed $CaCO_3$ surfaces provide abundant active sites for potential drug-loading applications and pH-responsive release capability. The resulting mesoporous architecture facilitates controlled diffusion kinetics, and the removal of protein components enhances biocompatibility. This synergistic combination of carbon matrix and calcium carbonate establishes a multifunctional platform that integrates high loading capacity with stimuli-responsive drug release properties for enhanced chemotherapeutic efficacy."

The nitrogen adsorption–desorption isotherms of the three samples (Fig. 5a and b) revealed critical impact into their surface area and pore structure, which are pivotal for evaluating their potential as nanodrug carriers. Notably, the isotherm of the PEG-coated eggshell powder after carbonization (C-PEG@ES) exhibited a typical Type IV adsorption–desorption profile, indicative of a well-developed mesoporous structure. In contrast, the untreated PEG-coated eggshell particles displayed no hysteresis loop, while the ultrafine eggshell particles showed a minor hysteresis loop. This distinct divergence in hysteresis behavior can be attributed to the role of PEG in encapsulating the eggshell particles, which effectively blocked the interparticle stacking pores. According to the updated IUPAC classification, the pronounced hysteresis loop observed in the C-PEG@ES sample aligns with the H3-type, typically associated with slit-like pores, wedge-shaped structures, or plate-like configurations. These findings suggest the formation of a porous architecture within the material. The observed porous architecture originates from the carbonized PEG layer formed during high-

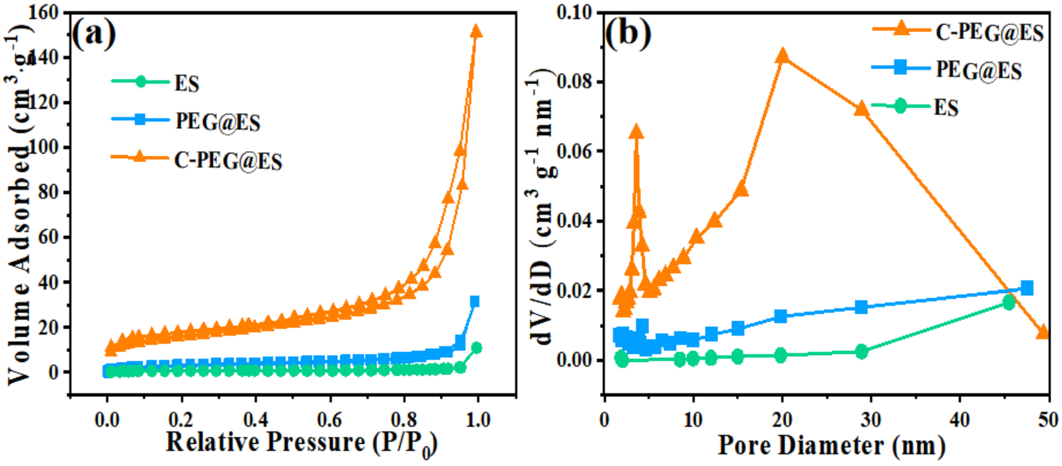

Fig. 5 (a) Nitrogen adsorption–desorption isotherms, (b) distribution curves.

temperature treatment, which adheres to the eggshell particle surface. The mesoporous carbon layer provides high specific surface areas for drug adsorption, while the interconnected pore network could facilitate the potential for drug loading. These structural features collectively highlight the promising drug delivery potential of the synthesized C-PEG@ES material. The pore size distribution, derived from the adsorption branch of the nitrogen isotherms in Fig. 5b, further elucidates the properties of the samples. For fine eggshell powder, the broad pore distribution arises from the interparticle stacking of fine particles. Upon PEG coating, the adhesion between particles significantly reduces these interparticle voids, as evidenced by the diminished pore volume. Remarkably, after high-temperature carbonization, the C-PEG@ES sample exhibits two distinct pore size peaks at 5 nm and 20 nm, with an average pore diameter of 15.5 nm. This distribution confirms the formation of a porous carbon layer derived from the thermal decomposition of PEG on the eggshell surface, corroborating the abundant mesoporous structure.

Table 1 summarizes the specific surface area and pore volume data for the three samples. The ultrafine eggshell powder exhibits a relatively large surface area of 12.3 $m^2\ g^{-1}$ after crushing and superfine. However, PEG coating induces particle agglomeration, drastically reducing the surface area by over 70% to 3.5 $m^2\ g^{-1}$. Remarkably, thermal treatment reverses this trend, the carbonization of PEG generates a porous carbon film on the eggshell surface, amplifying the surface area to 75.6 $m^2\ g^{-1}$—a sixfold increase compared to the pristine eggshell. This enhancement aligns with the pore volume data, the carbonized sample shows a 59-fold rise in micropore volume and a 12-fold increase in mesopore volume compared to the untreated PEG-coated sample. The mesoporous carbon layer and the increased surface area provides ample space for drug adsorption. These structural advantages strongly suggest that C-PEG@ES could achieve high drug-loading capacities as a promising candidate for drug delivery.

As shown in Fig. 6a, the drug loading capacity of both C-PEG@ES and ES increased over time. The drug loading of ES reached a maximum of 18.03% at 30 min, while that of C-PEG@ES gradually plateaued at 80 min with a loading capacity of 57.79%. These results indicate that, compared to pristine ES, the C-PEG@ES composite possesses a more porous structure and greater availability of surface active sites, resulting in continuous adsorption of more oxaliplatin (OXA) over time. After 80 min, the number of available adsorption sites on C-PEG@ES decreased significantly, and further increasing the loading time did not notably enhance the drug loading, indicating that equilibrium had been reached. The significantly improved drug loading capacity of C-PEG@ES demonstrates its promising potential as an efficient drug carrier.

Table 1 Surface area and porous structure parameters of ES, PEG@ES, and C-PEG@ES

Sample	ES	PEG-ES	C-PEG-ES
Surface area ($m^2\ g^{-1}$)	12.3	3.5	75.6
Average pore size (nm)	19.4	36.8	15.5
Micropore volume ($cm^3\ g^{-1}$)	0.003	0.001	0.06
Mesoporous volume ($cm^3\ g^{-1}$)	0.068	0.024	0.285
Total pore volume ($cm^3\ g^{-1}$)	0.071	0.025	0.345

The time-dependent pH changes of PBS solutions after Addition of C-PEG@ES at different initial pH values are shown in the Fig. 6b. When the initial pH was 7.4, the pH of the solution remained largely constant, indicating minimal decomposition of C-PEG@ES and demonstrating its high stability under physiological conditions. Notably, at pH 6.7(representative of the typical tumor extracellular microenvironment), the system effectively elevated the pH to 7.1, demonstrating its significant modulation capacity under mildly acidic conditions. At an initial pH of 6.2, the pH gradually increased over time, reaching 7.0 after 5 hours, suggesting partial decomposition of C-PEG@ES and its moderating effect on the acidity of the solution. With a further decrease in initial pH to 5.0, the pH increase became more pronounced, rising to 6.2 within 15 hours, which reflects enhanced decomposition under more acidic conditions. These results confirm the pH-responsive behavior of C-PEG@ES and highlight its potential to modulate the acidic tumor microenvironment.

To evaluate the drug release behavior of the C-PEG@ES nanocarrier system, *in vitro* simulated tests were conducted under varying pH conditions. First, the calcium ion (Ca^{2+}) release profile of the C-PEG@ES composite was investigated under varying pH conditions. Four pH values were selected: pH 5.0 (mimicking the acidic tumor microenvironment), pH 7.4 (simulating normal physiological conditions), pH 6.7(representative of the typical tumor extracellular microenvironment) and an intermediate pH 6.2. As shown in Fig. 6c, Ca^{2+} release exhibited strong pH dependence, with significantly accelerated dissolution rates under acidic conditions. Specifically, the cumulative Ca^{2+} release at pH 5.0 far exceeded that at pH 7.4 over the same time interval. This behavior is attributed to the rapid dissolution of the internal $CaCO_3$ component in acidic environments. These results suggest that the C-PEG@ES composite can selectively degrade in the tumor microenvironment, releasing the loading drug while simultaneously neutralizing the acidic microenvironment through $CaCO_3$ dissolution. This pH-modulating effect may further inhibit tumor cell invasion. Notably, at pH 6.7, the Ca^{2+} release reached approximately 165 ppb, demonstrating a moderate but significant response between the acidity of the typical tumor extracellular microenvironment and the C-PEG@ES composite.

Subsequently, the pH-dependent drug release kinetics of the C-PEG@ES system were analyzed using OXA (Fig. 6d). At pH 7.4 (normal tissue conditions), drug release was negligible, demonstrating the system's stability under physiological conditions. In contrast, a rapid and sustained drug release was observed at pH 5.0 (tumor microenvironment), with the cumulative release reaching 80%. The minimal release at pH 7.4 ensures targeted delivery to tumor sites, while the accelerated release under acidic conditions enhances therapeutic efficacy. At the tumor extracellular pH of 6.7, the system showed moderate yet substantial drug release, achieving approximately 45% cumulative release, indicating its responsive behavior even

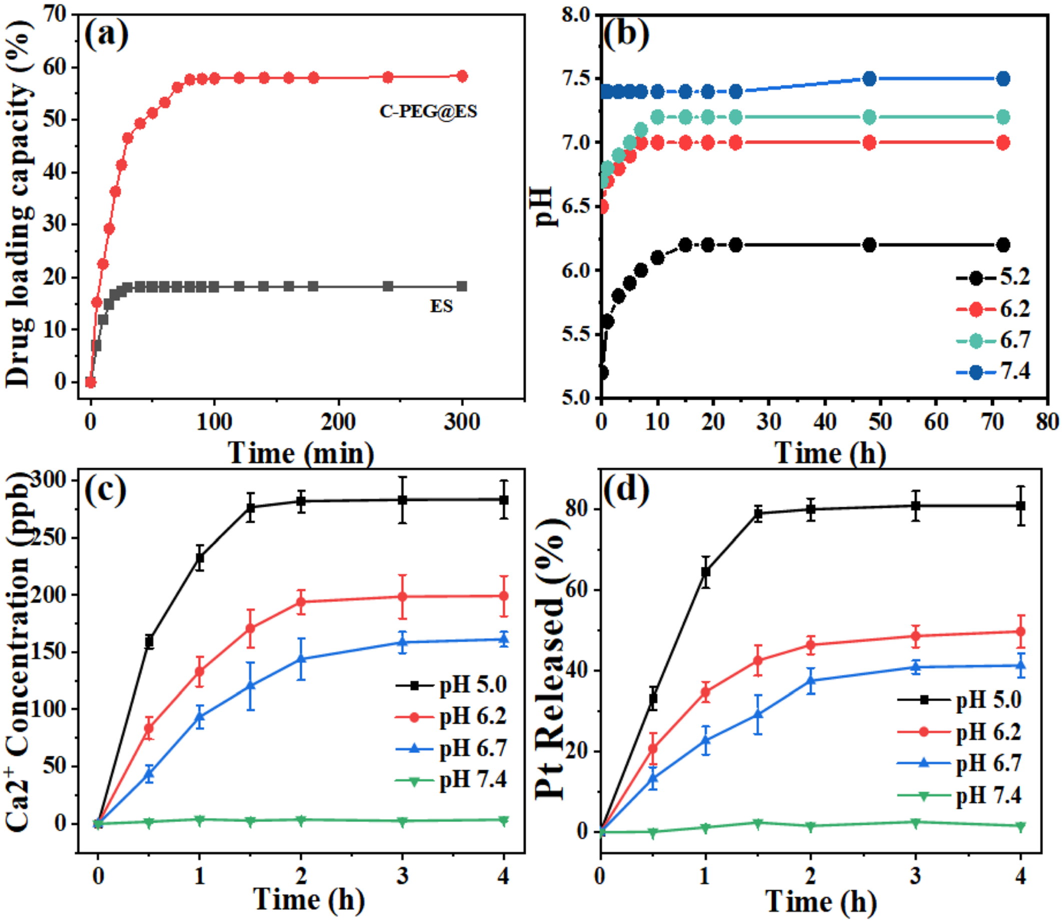

Fig. 6 (a) Drug loading capacity of C-PEG@ES, (b) pH change with different initial pH values over time, (c) release profiles of Ca^{2+} from C-PEG@ES, (d) release profiles of Pt from C-PEG@ES.

in mildly acidic conditions. These findings highlight the pH-responsive drug release behavior of the C-PEG@ES, enabling tumor-specific delivery. Besides, its $CaCO_3$ component acts as a microenvironment modulator to inhibit tumor cell invasion.

When nanocarriers enter human tissue fluid, they attract proteins that assemble into an adsorption layer on their surface, a unique structure known as the "protein corona" (PC). The protein corona not only alters the physicochemical properties of the nanocarriers but also directly affects their biological behavior.[38–42] To investigate the potential impact of protein corona formation on drug release kinetics, we conducted supplementary experiments by preparing PBS solutions supplemented with fetal bovine serum to simulate the physiological environment. The drug release profiles were systematically evaluated under these physiologically relevant conditions(Fig. 7). As shown in Fig. 7, the cumulative drug release from protein corona-coated carriers reached approximately 48.1%, compared to their non-corona counterparts. During the initial 2-hour period, the corona-formed samples demonstrated significantly slowed release kinetics, with substantially lower release amounts than the control group. However, over time, the release profile gradually approached that of the control, with the difference between the two continuously diminishing. Overall, the formation of the protein corona reduced the cumulative release of OXA by approximately 5% and notably slowed the drug release kinetics.

Overall, the performance of our material is competitive with that of other advanced nanocarriers reported in the literature (Table 2).[14,43–47]

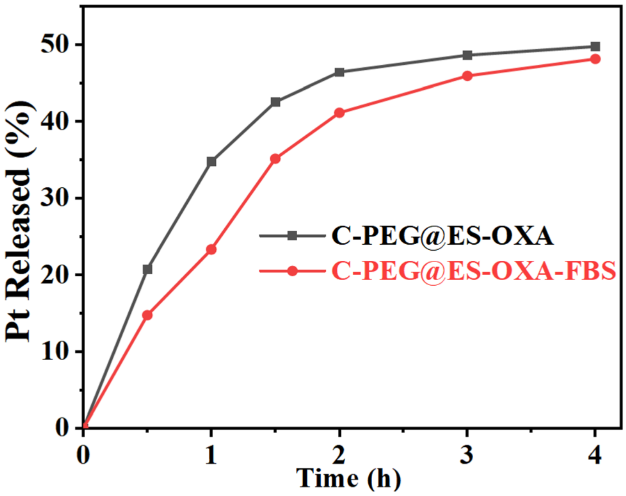

Fig. 7 Release profiles of Pt from C-PEG@ES and C-PEG@ES-FBS.

Table 2 Surface area, porous structure parameters and the release behavior of C-PEG@ES and other similar reported nanocarriers based $CaCO_3$ and carbon

Sample	Surface area ($m^2\ g^{-1}$)	Average pore diameter (nm)	The release behavior of drug (pH5.0)	Ref.
N2HMCN	162	6.17	33%	14
ACC	360	8–9	90%	43
$CaCO_3$/GG	113	3–30	68%	44
Micro-CNs	435	2.5	35%	45
PAA-CD-$CaCO_3$	36	23	30%	46
$^{PGF}CaCO_3$-PEG	—	—	76.6%	47
C-PEG-ES	75.6	15.5	80%	This work

This study systematically evaluated the biocompatibility of C-PEG@ES nanomaterials and the antitumor efficacy of its drug-loaded system using BMSC, UMR-106, and CT26 cell models, with cell viability assessed by the CellTiter-Glo (CTG) assay. As shown in Fig. 8a, the pristine C-PEG@ES nanomaterials maintained cell viability above 95% after 24 and 48 hours of co-culture with BMSCs, demonstrating minimal cytotoxicity and excellent biocompatibility. The cytotoxicity of C-PEG@ES-OXA and C-PEG@ES-DOX systems against UMR-106 and CT26 cells was further investigated. Both drug-loaded systems significantly reduced cell viability. After 24 hours of co-culture with C-PEG@ES-OXA, the viability of CT26 and UMR-106 cells decreased to approximately 50% and 42%, respectively, indicating substantial antitumor efficacy with a more pronounced effect on UMR-106 cells. In comparison, treatment with C-PEG@ES-DOX for 24 hours resulted in viability rates of approximately 45% for CT26 cells and 50% for UMR-106 cells, demonstrating stronger antitumor activity against CT26 cells.

As shown in Fig. 8b, BMSCs cultured in control medium and C-PEG@ES-containing medium exhibited robust proliferation, with the majority of cells displaying green fluorescence (indicating high viability) and minimal red fluorescence signal (indicating dead cells). This further confirms the minimal biotoxicity and good cytocompatibility of the drug carrier toward normal cells.

The live/dead cell staining assay further confirmed the antitumor efficacy of C-PEG@ES-OXA and C-PEG@ES-DOX. As shown in Fig. 9, both CT26 and UMR-106 cells cultured in

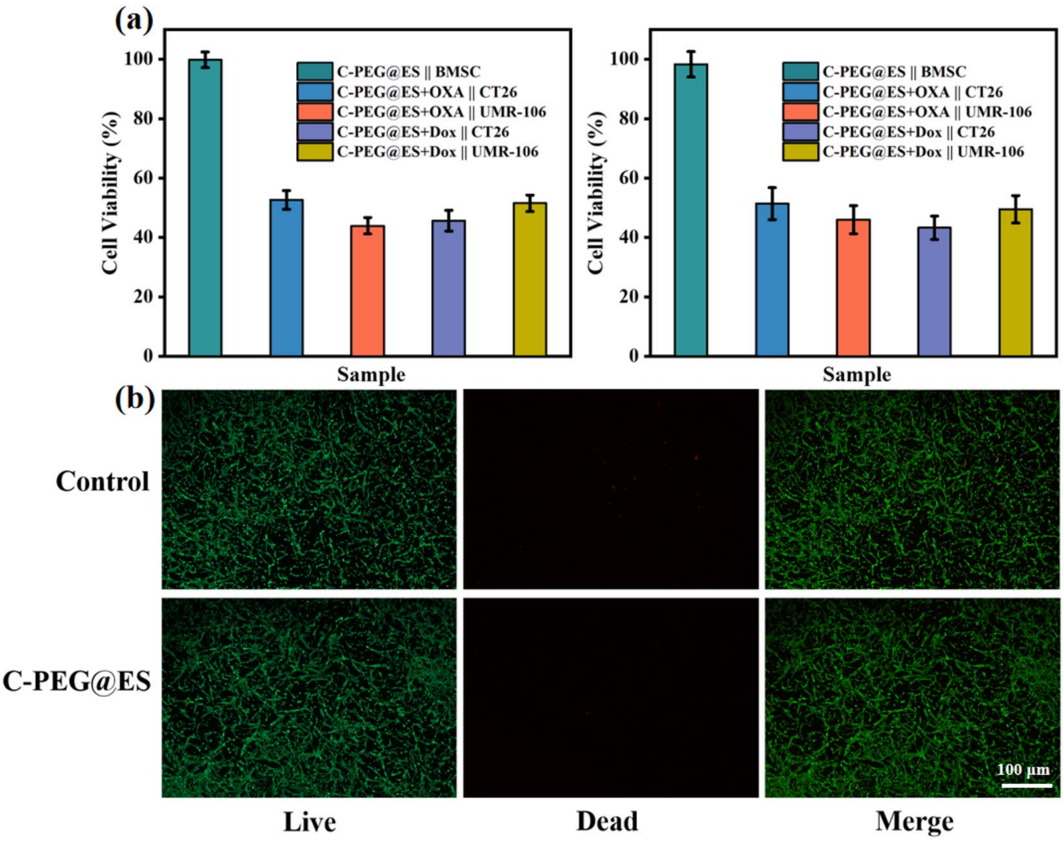

Fig. 8 (a) Cell viability assays of BMSC, UMR-106 and CT26, (b) live-dead staining of BMSC treated with control and C-PEG@ES.

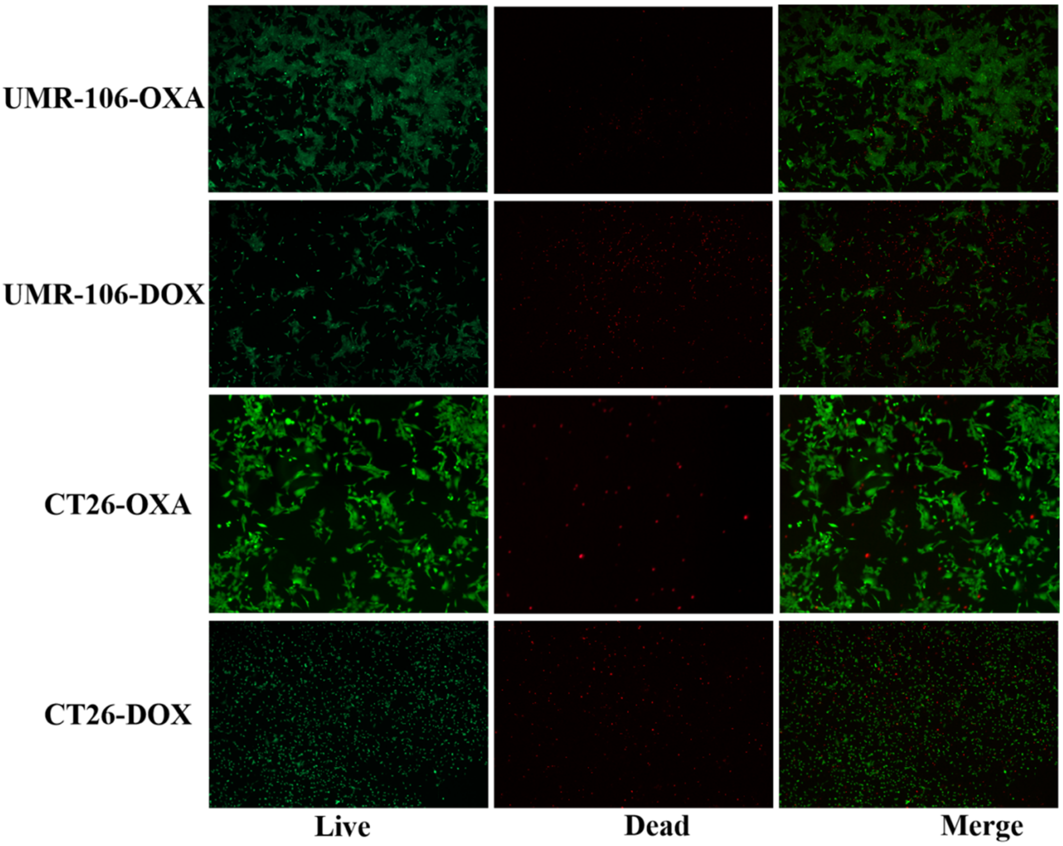

Fig. 9 Live-dead staining of UMR-106 and CT26 cells treated with C-PEG@ES-OXA and C-PEG@ES-DOX.

medium containing C-PEG@ES-OXA exhibited significant apoptosis. Compared with Fig. 8b, a notable reduction in green fluorescence and increased red fluorescence signals were observed. Furthermore, UMR-106 cells showed lower viability than CT26 cells, as indicated by a more pronounced increase in red fluorescence accompanied by a simultaneous decrease in green fluorescence. These results further demonstrate the stronger cytotoxic effect of OXA against UMR-106 cells. Similarly, both CT26 and UMR-106 cells treated with C-PEG@ES-DOX also displayed substantial apoptosis. In contrast to the OXA-loaded system, CT26 cells showed lower viability than UMR-106 cells, with markedly enhanced red fluorescence and weakened green fluorescence. These findings confirm that DOX exhibits stronger killing activity against CT26 cells. The differential cytotoxicity profiles of C-PEG@ES loaded with different drugs highlight its great potential as a versatile drug carrier. Moreover, the robust tumor-killing efficacy exhibited by drug-loaded C-PEG@ES against various cancer cell types suggests broad application prospects in the field of cancer therapy.

4. Conclusion

In summary, biomass waste eggshells were utilized as a calcium carbonate source to construct a carbonaceous chrysalis-like structure. By coating the eggshell core with polyethylene glycol (PEG) followed by carbonization, a loose and porous carbon-based drug carrier (C-PEG@ES) was successfully fabricated for tumor-targeted drug delivery. The prepared C-PEG@ES nanomaterial demonstrated pH-responsive drug release behavior in the weakly acidic tumor microenvironment, where the decomposition of $CaCO_3$ accelerated drug release and synergistically induced cancer cell apoptosis. Additionally, the $CaCO_3$ component neutralized the acidic tumor microenvironment, effectively inhibiting cancer cell invasion into adjacent normal tissues. This work provides a sustainable strategy for developing eco-friendly, pH-responsive drug carriers using biowaste-derived materials, showing promising potential for precision cancer therapy.

Conflicts of interest

The authors declare that they have no known competing financial interests or personal relationships that could have appeared to influence the work reported in this paper.

Data availability

Data available on request from the authors.

Acknowledgements

This research is financially supported by Natural Science Foundation of China Jiangsu Province (BK20230940 and BK20243017), and a project funded by Jiangsu Funding

Program for Excellent Postdoctoral Talent. We acknowledge the analytical facilities support in the Center of Analytical Facilities, Nanjing University of Science and Technology.

References

1 C. De Martel, D. Georges, F. Bray, *et al.*, Global burden of cancer attributable to infections in 2018: a worldwide incidence analysis, *Lancet Global Health*, 2020, **8**(2), e180–e190.

2 R. L. Siegel, K. D. Miller, N. S. Wagle, *et al.*, Cancer statistics, 2023, *Ca-Cancer J. Clin.*, 2023, **73**(1), 17–48.

3 H. Sung, J. Ferlay, R. L. Siegel, *et al.*, Global Cancer Statistics 2020: GLOBOCAN Estimates of Incidence and Mortality Worldwide for 36 Cancers in 185 Countries, *Ca-Cancer J. Clin.*, 2021, **71**(3), 209–249.

4 F. Mahmoudian, A. Ahmari, S. Shabani, *et al.*, Aptamers as an approach to targeted cancer therapy, *Cancer Cell Int.*, 2024, **24**(1), 108.

5 J. Feng, B. Li, J. Ying, *et al.*, Liquid Biopsy: Application in Early Diagnosis and Monitoring of Cancer, *Small Struct.*, 2020, **1**(3), 2000063.

6 E. Bozzato, C. Bastiancich and V. Preat, Nanomedicine: A Useful Tool against Glioma Stem Cells, *Cancers*, 2020, **13**(1), 9.

7 R. G. Kenny and C. J. Marmion, Toward Multi-Targeted Platinum and Ruthenium Drugs-A New Paradigm in Cancer Drug Treatment Regimens?, *Chem. Rev.*, 2019, **119**(2), 1058–1137.

8 K. Ganesh and J. Massague, Targeting metastatic cancer, *Nat. Med.*, 2021, **27**(1), 34–44.

9 D. Gulwani, P. Upadhyay, R. Goel, *et al.*, Nanomedicine mediated thyroid cancer diagnosis and treatment: an approach from generalized to personalized medicine, *Discov. Oncol.*, 2024, **15**(1), 789.

10 Q. Zhang, G. Kuang, S. He, *et al.*, Photoactivatable Prodrug-Backboned Polymeric Nanoparticles for Efficient Light-Controlled Gene Delivery and Synergistic Treatment of Platinum-Resistant Ovarian Cancer, *Nano Lett.*, 2020, **20**(5), 3039–3049.

11 Brianna and S. H. Lee, Chemotherapy: how to reduce its adverse effects while maintaining the potency?, *Med. Oncol.*, 2023, **40**(3), 88.

12 Y. Xu, C. Wang, F. Shen, *et al.*, Lipid-Coated $CaCO_{(3)}$ Nanoparticles as a Versatile pH-Responsive Drug Delivery Platform to Enable Combined Chemotherapy of Breast Cancer, *ACS Appl. Bio Mater.*, 2022, **5**(3), 1194–1201.

13 M. Xu, J. Zhang, Y. Mu, *et al.*, Activation of TRPV1 by capsaicin-loaded $CaCO_{(3)}$ nanoparticle for tumor-specific therapy, *Biomaterials*, 2022, **284**, 121520.

14 V. Lauth, B. Loretz, C.-M. Lehr, *et al.*, Self-Assembly and Shape Control of Hybrid Nanocarriers Based on Calcium Carbonate and Carbon Nanodots, *Chem. Mater.*, 2016, **28**(11), 3796–3803.

15 G. F. Luo, X. D. Xu, J. Zhang, *et al.*, Encapsulation of an adamantane-doxorubicin prodrug in pH-responsive polysaccharide capsules for controlled release, *ACS Appl. Mater. Interfaces*, 2012, **4**(10), 5317–5324.

16 J. Li, H. Jiang, X. Ouyang, *et al.*, $CaCO_{(3)}$/Tetraethylenepentamine-Graphene Hollow Microspheres as Biocompatible Bone Drug Carriers for Controlled Release, *ACS Appl. Mater. Interfaces*, 2016, **8**(44), 30027–30036.

17 M. Q. Gong, J. L. Wu, B. Chen, *et al.*, Self-assembled polymer/inorganic hybrid nanovesicles for multiple drug delivery to overcome drug resistance in cancer chemotherapy, *Langmuir*, 2015, **31**(18), 5115–5122.

18 C. Zhang, S. Li, A. Yu, *et al.*, Nano $CaCO_{(3)}$ "Lysosomal Bombs" Enhance Chemotherapy Drug Efficacy *via* Rebalancing Tumor Intracellular pH, *ACS Biomater. Sci. Eng.*, 2019, **5**(7), 3398–3408.

19 Y. Ma, J. Huang, S. Song, *et al.*, Cancer-Targeted Nanotheranostics: Recent Advances and Perspectives, *Small*, 2016, **12**(36), 4936–4954.

20 Z. Dong, L. Feng, W. Zhu, *et al.*, $CaCO_{(3)}$ nanoparticles as an ultra-sensitive tumor-pH-responsive nanoplatform enabling real-time drug release monitoring and cancer combination therapy, *Biomaterials*, 2016, **110**, 60–70.

21 H. Bahrom, A. A. Goncharenko, L. I. Fatkhutdinova, *et al.*, Controllable Synthesis of Calcium Carbonate with Different Geometry: Comprehensive Analysis of Particle Formation, Cellular Uptake, and Biocompatibility, *ACS Sustain. Chem. Eng.*, 2019, **7**(23), 19142–19156.

22 D. A. Eurov, D. A. Kurdyukov, V. M. Boitsov, *et al.*, Biocompatible acid-degradable micro-mesoporous $CaCO_3$:Si:Fe nanoparticles potential for drug delivery, *Microporous Mesoporous Mater.*, 2022, 333.

23 Y. Zhang, L. Cai, D. Li, *et al.*, Tumor microenvironment-responsive hyaluronate-calcium carbonate hybrid nanoparticle enables effective chemotherapy for primary and advanced osteosarcomas, *Nano Res.*, 2018, **11**(9), 4806–4822.

24 B. N. Yalamandala, Y.-J. Chen, Y.-H. Lin, *et al.*, A Self-Cascade Penetrating Brain Tumor Immunotherapy Mediated by Near-Infrared II Cell Membrane-Disrupting Nanoflakes *via* Detained Dendritic Cells, *ACS Nano*, 2024, **18**(28), 18712–18728.

25 M.-R. Chiang, C.-W. Hsu, W.-C. Pan, *et al.*, Reprogramming Dysfunctional Dendritic Cells by a Versatile Catalytic Dual Oxide Antigen-Captured Nanosponge for Remotely Enhancing Lung Metastasis Immunotherapy, *ACS Nano*, 2024, **19**(2), 2117–2135.

26 T. Moorthy, C.-K. Chen, Z.-H. Liu, *et al.*, Wireless chargeable gold Yarnball-mediated mitochondrial depolarization for dendritic cell detainment in programmed brain tumor immunotherapy, *Nano Today*, 2025, **65**, 102838.

27 T. M. H. Huynh, P.-X. Huang, K.-L. Wang, *et al.*, Reprogramming Immunodeficiency in Lung Metastases *via* PD-L1 siRNA Delivery and Antigen Capture of Nanosponge-Mediated Dendritic Cell Modulation, *ACS Nano*, 2025, **19**(27), 25134–25153.

28 M. Pourmadadi, H. Abdouss, A. Memarzadeh, *et al.*, Innovative chitosan-polyacrylic acid-MoS_2 nanocomposite

for enhanced and pH-responsive quercetin delivery, *Mater. Today Commun.*, 2024, **39**, 108724.

29 M. Shirzad, A. Salahvarzi, S. Fathi-karkan, *et al.*, Green nanocarriers and Biodegradable Systems for sustainable drug delivery solutions, *J. Drug Delivery Sci. Technol.*, 2025, 111.

30 S. Fathi-karkan, S. Nasiri, M. Hasannia, *et al.*, Green carbon dots and theranostic applications, *J. Drug Delivery Sci. Technol.*, 2025, 108.

31 S. M. Kawish, S. Sharma, P. Gupta, *et al.*, Nanoparticle-Based Drug Delivery Platform for Simultaneous Administration of Phytochemicals and Chemotherapeutics: Emerging Trends in Cancer Management, *Part. Part. Syst. Charact.*, 2024, **41**(12), 2400049.

32 I. H. Alsohaimi, A. M. Nassar, T. A. Seaf elnasr, *et al.*, A novel composite silver nanoparticles loaded calcium oxide stemming from egg shell recycling: a potent photocatalytic and antibacterial activities, *J. Cleaner Prod.*, 2020, 248.

33 K. Yorseng, S. Siengchin, B. Ashok, *et al.*, Nanocomposite egg shell powder with *in situ* generated silver nanoparticles using inherent collagen as reducing agent, *J. Bioresour. Bioprod.*, 2020, **5**(2), 101–107.

34 P. Chuysinuan, P. Nooeaid, T. Thanyacharoen, *et al.*, Injectable eggshell-derived hydroxyapatite-incorporated fibroin-alginate composite hydrogel for bone tissue engineering, *Int. J. Biol. Macromol.*, 2021, **193**(Pt A), 799–808.

35 A. Shafiu Kamba, M. Ismail, T. A. Tengku Ibrahim, *et al.*, A pH-sensitive, biobased calcium carbonate aragonite nanocrystal as a novel anticancer delivery system, *BioMed Res. Int.*, 2013, **2013**, 587451.

36 S. Jain, S. M. Dongave, T. Date, *et al.*, Succinylated beta-Lactoglobuline-Functionalized Multiwalled Carbon Nanotubes with Improved Colloidal Stability and Biocompatibility, *ACS Biomater. Sci. Eng.*, 2019, **5**(7), 3361–3372.

37 B. M. Chen, T. L. Cheng and S. R. Roffler, Polyethylene Glycol Immunogenicity: Theoretical, Clinical, and Practical Aspects of Anti-Polyethylene Glycol Antibodies, *ACS Nano*, 2021, **15**(9), 14022–14048.

38 Q. Xiao, M. Zoulikha, M. Qiu, *et al.*, The effects of protein corona on *in vivo* fate of nanocarriers, *Adv. Drug Delivery Rev.*, 2022, 186.

39 Y.-R. Wu, Q. Zhou, J. Li, *et al.*, The formation of protein coronas and its effect on the quercetin-edible dock protein nanoparticles, *Food Hydrocolloids*, 2024, **157**, 110432.

40 G. Caracciolo, Artificial protein coronas: directing nanoparticles to targets, *Trends Pharmacol. Sci.*, 2024, **45**(7), 602–613.

41 P. C. Ke, S. Lin, W. J. Parak, *et al.*, A Decade of the Protein Corona, *ACS Nano*, 2017, **11**(12), 11773–11776.

42 K. E. Wheeler, A. J. Chetwynd, K. M. Fahy, *et al.*, Environmental dimensions of the protein corona, *Nat. Nanotechnol.*, 2021, **16**(6), 617–629.

43 H. Yang, Y. Wang, T. Liang, *et al.*, Hierarchical porous calcium carbonate microspheres as drug delivery vector, *Prog. Nat. Sci.:Mater. Int.*, 2017, **27**(6), 674–677.

44 R. Sun, P. Zhang, É. G. Bajnóczi, *et al.*, Amorphous Calcium Carbonate Constructed from Nanoparticle Aggregates with Unprecedented Surface Area and Mesoporosity, *ACS Appl. Mater. Interfaces*, 2018, **10**(25), 21556–21564.

45 Y. Han, Z. Dong, C. Wang, *et al.*, Ferrous ions doped calcium carbonate nanoparticles potentiate chemotherapy by inducing ferroptosis, *J. Controlled Release*, 2022, **348**, 346–356.

46 L. Zhou, Y. Jing, Y. Liu, *et al.*, Mesoporous Carbon Nanospheres as a Multifunctional Carrier for Cancer Theranostics, *Theranostics*, 2018, **8**(3), 663–675.

47 S. Asgari, A. Pourjavadi, S. H. Hosseini, *et al.*, A pH-sensitive carrier based-on modified hollow mesoporous carbon nanospheres with calcium-latched gate for drug delivery, *Mater. Sci. Eng., C*, 2020, 109.